JGR Space Physics

Key Points:

- Relativistic electron precipitation (REP) events detected using POES/MetOp 2 s data show the expected distributions in L and magnetic local time (MLT)
- The 2 s data offers greater spatial resolution than in previous studies, and reveals that REP events are narrow in L shell
- Spatial structure during long midnight REP events may point to multiple mechanisms acting around midnight MLT

Correspondence to:

L. C. Gasque,
lcgasque@berkeley.edu

Statistically Determining the Spatial Extent of Relativistic Electron Precipitation Events Using 2-s Polar-Orbiting Satellite Data

L. Claire Gasque[1] , **Robyn M. Millan[2]** , **and Sapna Shekhar[3]**

[1]Physics Department and Space Sciences Lab, University of California, Berkeley, CA, USA, [2]Department of Physics and Astronomy, Dartmouth College, Hanover, NH, USA, [3]Department of Physics, Auburn University, Auburn, AL, USA

Abstract Relativistic electron precipitation (REP) from the outer radiation belt into Earth's atmosphere poses risks for satellites and affects Earth's climate, producing ozone-destroying compounds. Characterizing the spatial extent of REP events, which are periods of precipitation localized in space and time, is important for quantifying these effects and improving understanding of outer radiation belt dynamics, allowing quantification of the relative roles of atmospheric and magnetopause particle loss. Following Shekhar et al. (2017, https://doi.org/10.1002/2017JA024716), who used 16 s resolution data from particle detectors onboard NOAA's Polar-orbiting Operational Environmental Satellites (POES) and the ESA's Meterological Operational (MetOp) Satellites, we work to more precisely determine the spatial extent of REP events using higher-resolution (2 s) data from the same instruments. We algorithmically search through 6 years of data (October 2012 to December 2018) from a maximum of seven simultaneously orbiting satellites, identifying REP events and determining their start and end times and locations. We find that the majority of events are highly localized spatially and, unlike Shekhar et al. (2017, https://doi.org/10.1002/2017JA024716), we do not observe a cluster of broad events around midnight magnetic local time (MLT). Based on case studies, we suggest that this discrepancy results from the differences in data resolution, indicating that the broad regions of precipitation around midnight MLT identified by Shekhar et al. (2017, https://doi.org/10.1002/2017JA024716) may be composed of several adjacent but narrowly confined regions of precipitation, potentially with independent causes. Additional work is necessary to further classify events and identify their likely mechanisms.

1. Introduction

Within Earth's magnetosphere lie the Van Allen radiation belts, surrounding the Earth with energetic, charged particles. Under typical geomagnetic conditions, there are two such belts—a relatively stable inner belt, and a dynamic outer belt composed of electrons and low-energy protons, typically confined within $3 \leq L \leq 8$ (e.g., Millan & Baker, 2012; Millan & Thorne, 2007). Outer belt electrons with relativistic energies often remain trapped by Earth's magnetic field for less than a day before either escaping across the magnetopause or precipitating into Earth's atmosphere (Thorne et al., 2005). Precipitating electrons can degrade shortwave radio signals (Evans & Greer, 2000), damage satellite instrumentation (Horne et al., 2013), and produce compounds capable of destroying mesospheric and stratospheric ozone (e.g., Brasseur & Solomon, 2005; Randall et al., 2005). Quantifying the size of the region over which relativistic electron precipitation (REP) occurs will improve understanding of the dynamics in the outer radiation belt, informing future radiation belt and climate models.

If a particle's equatorial pitch angle is small enough that its mirror point lies within Earth's atmosphere ($<\sim$100 km above the surface), the particle will likely collide with atmospheric particles and precipitate (Millan & Baker, 2012). Particles are defined to be in the bounce loss cone (BLC) if they will enter the atmosphere within a single bounce period (Selesnick, 2006). Mechanisms such as wave-particle interactions can cause pitch angle scattering, changing affected particle pitch angles, and causing particles that were previously trapped to instead enter the BLC (Millan & Thorne, 2007). Waves capable of pitch angle scattering relativistic electrons include whistler-mode plasmaspheric hiss and chorus, and electromagnetic ion-cyclotron (EMIC) waves (Meredith et al., 2003; Shprits et al., 2008; Summers et al., 1998). Since relativistic
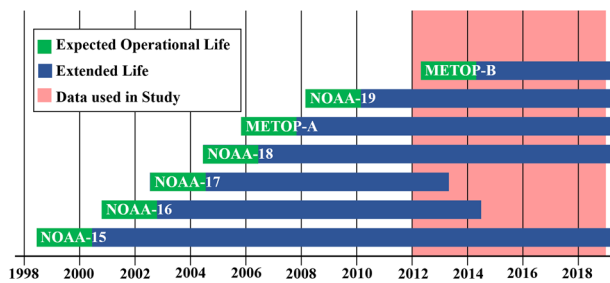
Figure 1. Timeline of NOAA POES satellites as used in this study. Note that each satellite had an expected operational life of 2 years after launch, shown in green, followed by an extended life, shown in blue. The 2 s resolution data used in this study is currently available for only the period highlighted in red.

electrons drift rapidly around the Earth, they may interact with several types of waves in a single orbit (Rodger et al., 2010).

Shekhar et al. (2017) recently investigated the spatial extent of REP events using 16 s resolution data from NOAA's Polar-orbiting Operational Environmental Satellites (POES) and the ESA's Meterological Operational (MetOp) Satellites from 2000 to 2014. They reported two classes of REP events. The first was localized in L and coincided with low-energy proton precipitation, as might be expected from EMIC wave-driven precipitation (Carson et al., 2013). These events were concentrated in the dusk and early morning sectors MLT. Second, they found a class of events near midnight MLT which were broad in L shell and did not coincide with low-energy proton precipitation. These were theorized to be caused by current sheet scattering in the tail of the magnetic field, which occurs under geomagnetically active conditions.

This work directly follows Shekhar et al. (2017), using 2 s POES/MetOp data (available since 2012) to improve resolution and sensitivity of REP event detections. Using this higher-resolution data, this work aims to confirm whether there are, indeed, multiple clusters of events characterized by size, as well as investigate the spatial structure of these events. We will also examine a case study of an event in direct comparison with Shekhar et al. (2017) to investigate the substructure of longer events around midnight MLT.

In Section 2, we describe both the data source and our REP event detection algorithm. In Section 3, we present the results of the statistical analysis as well as the case study. Finally, in Section 4, we conclude and discuss potential future work.

2. Data and Methods

2.1. POES/MetOp Satellites and Instrumentation

This work uses data from the second generation Space Environment Monitoring (SEM-2) subsystem onboard the POES/MetOp satellites. These satellites' primary purpose is environmental modeling and weather forecasting, but because of the SEM-2 subsystem, they have generated one of the most important long-term space physics data sets for studying energetic particles (Asikainen et al., 2012; Nesse Tyssøy et al., 2016; Peck et al., 2015; Van de Kamp et al., 2016).

Both the POES and MetOp satellites have sun-synchronous polar orbits with a period of ∼102 min (Evans & Greer, 2000). As a result, the satellites move across L shells while their MLT stays nearly constant. The satellites each have a different MLT coverage, allowing broad (if slightly biased) coverage in L and MLT.

The satellites orbit at about 870 km above the Earth's surface and are stabilized such that their spatial orientation is fixed relative to both their direction of travel and the local zenith (Evans & Greer, 2000). Loss cone particles are easily viewed by measurements made near the foot of the magnetic field lines, making these satellites suitable for studying particle precipitation (Rodger et al., 2010).

This work uses satellite data from 2012 to 2018, during which a maximum of seven satellites were in orbit simultaneously, providing complete global coverage every 6 h. Figure 1 shows when each of the satellites used in this work were in operation.

The Space Environment Monitoring 2 (SEM-2) subsystem contains several sets of instruments and is designed to monitor charged particle fluxes. For this work, we used the Medium Energy Proton and Electron Detectors (MEPED) (Data from these instruments is available at 2 s cadence since 2012, and can be accessed from https://satdat.ngdc.noaa.gov/sem/poes/data/), a collection of solid-state particle detectors designed to separate particle species (electrons from protons) and measure the particle energies, sampling from two different directions (Green, 2013). MEPED measures protons in six different energy channels and electrons in three energy channels, with the nominal responses of each channel given in Table 1. These instruments

Table 1
MEPED Channel Nominal Energy Bands (Evans & Greer, 2000)

Channel Name	Particles Detected	Energy Range (keV)
P1	Protons	30−80
P2	Protons	80−240
P3	Protons	240−800
P4	Protons	800–2,500
P5	Protons	2,500–6,900
P6	Protons	>6900
E1	Electrons	30–2,500
E2	Electrons	100–2,500
E3	Electrons	300−2,500

sample from radiation belt populations, solar proton event particles, and lower energy cosmic rays (Evans & Greer, 2000).

MEPED measures particles in two nearly orthogonal directions, with a 0° telescope directed roughly toward the local zenith and a 90° telescope, directly roughly anti-parallel to the satellite's velocity (Carson et al., 2013). Both telescopes have a field-of-view of $\pm15°$. The telescopes alternate recording data, each integrating data for 1 s, giving a sampling rate of 2 s (Evans & Greer, 2000).

At high latitudes (above $L = 1.4$), where magnetic field lines extend nearly radially from the Earth, the 0° telescope points roughly along the magnetic field and observes only particles in the BLC, which are about to precipitate (Rodger et al., 2010). In this study, we examine only data from the 0° telescope at high latitudes. While the 90° telescope does observe precipitating particles at low latitudes, we are focusing on precipitation from the outer radiation belt, which occurs above an L of 3.

2.2. Event Selection Criteria

Given that we hope to identify all REP events in 6 years of data for up to seven simultaneously operating satellites, it was not feasible to identify each event by eye—it was necessary to write an algorithm to reliably extract events using a set of predetermined criteria. Using the MEPED channel responses to different energy particles as reported in Yando et al. (2011), we determine which channels should respond to REP events. We then evaluate the noise level in each of the channels in order to pick true events out from the background noise. We additionally impose several constraints to prevent false positive events.

2.2.1. MEPED Particle Channel Sensitivities

It is well-known that the MEPED P6 channel, designed to measure >6,900 keV protons, is contaminated by relativistic electrons, whose high energies allow them to reach the detector without being deflected by the cross-aperture magnetic field (Carson et al., 2013; Green, 2013). Previous studies have made use of this fact, using the P6 channel to detect and study REP events (e.g., Capannolo et al., 2019; Carson et al., 2013; Horne et al., 2009; Millan et al., 2010; Miyoshi et al., 2008; Peck et al., 2015; Qin et al., 2018; Rodger et al., 2010; Shekhar et al., 2017).

Yando et al. (2011) conducted a Monte Carlo simulation of the MEPED instruments to precisely determine their response to protons and electrons at different energies. The results of this analysis for the P5, P6, and E3 channels, which we will be using to develop our criteria, are shown in Figure 2. We note that the channel responses from Yando et al. (2011) do not account for instrument wear over time. Several studies have since provided additional flux corrections (e.g., Asikainen et al., 2012; Asikainen & Mursula, 2011; McFadden et al., 2007; Peck et al., 2015), but, as we are interested in only the extent of the precipitation regions and not precise fluxes, we did not take these into account for the present study.

As shown in Figure 2b, the P6 channel begins to respond significantly to electrons with energies above ∼800 keV, with an increasing response for more energetic electrons. In contrast, the P5 channel does not respond to electrons at all. If there are counts in the P5 channel, the detector is likely encountering high-energy protons, meaning that there is no way to guarantee that counts measured by the P6 channel are relativistic electrons. In the outer belt, high-energy protons are rare because, in the weaker magnetic field conditions, the proton gyroradii become too large for the
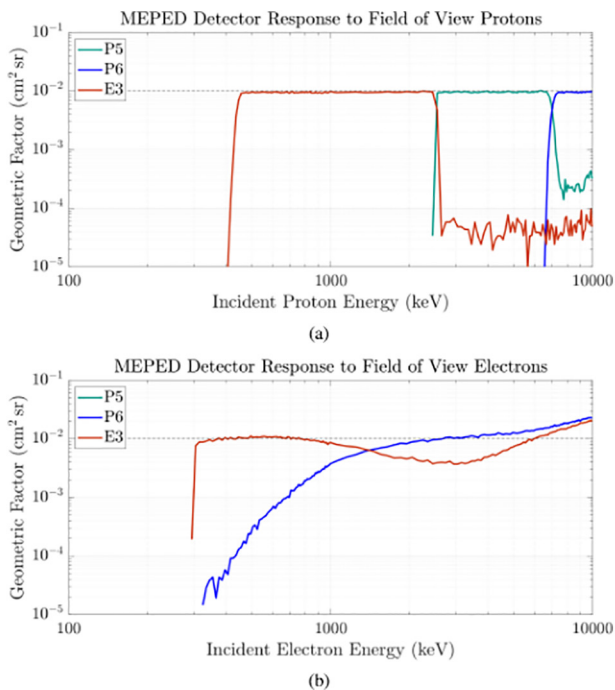

Figure 2. Geometric factors for the P5 (teal), P6 (blue), and E3 (red) MEPED channels for (a) protons and (b) electrons of various energies. Data courtesy of Karl Yando. MEPED, Medium Energy Proton and Electron Detectors.

particles to remain trapped (Lenchek & Singer, 1962; Sandanger et al., 2007). The detectors are only likely to encounter significant numbers of energetic protons during solar proton events. Thus, by disregarding events for which there are counts in the P5 channel, we can be more confident that we are truly observing REP. While other proton channels, including P2, P3, and P4, are also contaminated by high-energy electrons, P6 has the greatest response above 800 keV (Yando et al., 2011).

Note that, since E3 is an integral channel, measuring all electrons above 300 keV, the counts registered in E3 should almost always be greater than those in P6. However, if there were an REP event that only involved electrons greater than about 2 MeV, the P6 channel response would be greater since P6 has a larger geometric factor in this energy range. Precipitation is an energy-dependent process (O'Brien, 1964) and some mechanisms, such as EMIC waves, are thought to preferentially scatter higher-energy particles (Thorne & Andreoli, 1980), making this scenario plausible. However, as explained in Shekhar et al. (2017) and based on observations of a longitudinal bias in P6 not observed in E3 by Horne et al. (2009), sufficiently energetic particles not in the BLC may penetrate through the sides of the detector and register in the 0° telescope P6 channel, causing P6 counts to artificially exceed those in E3. The detector is shielded to prevent electrons of less than 6 MeV and protons of less than 90 MeV from penetrating through the sides, but sufficiently energetic particles may still get through, resulting in false counts (Evans & Greer, 2000). It is still unclear why these penetrating particles preferentially register in the P6 channel, but, as it is, we cannot be sure whether particles are truly in the BLC when P6 exceeds E3, so we therefore exclude those events.

2.2.2. Noise Analysis

As noted in Rodger et al. (2010), the P6 detector often reports counts near the instrument's noise floor, only reporting elevated counts during more intense events. To reliably extract only real events, we must first determine this noise threshold, which we do by modeling the background counts in each channel using a Poisson distribution. Looking only in the outer radiation belt region ($3.5 \leq L \leq 8$) during our period of interest, the average number of counts in the P6 channel is 0.65 counts per second, which is relatively consistent over time and across satellites.

Modeling this as a Poisson distribution with $\lambda = 0.65$ indicates that, in the ~76 million data points examined, we would expect no more than two false events with counts above 9 counts per second, which we adopt conservatively as our detection threshold for events that appear as only a single elevated spike in the data. For events that consist of more than one elevated point, we conservatively exclude all events with counts below 7 cps.

This is similar to, but slightly more strict than the approach taken by Yahnin et al. (2016), who looked through 38 days of 2 second data by eye and required events to exceed a noise floor of 5 cps to be considered real. However, Yahnin et al. (2016) excluded single point events, while we admit them if they have sufficiently elevated counts.

The noise level in the P5 channel is typically well below 2 cps. Thus, we exclude events during or near which counts in the P5 channel exceed 2 cps to avoid falsely considering solar energetic protons or contamination from the SAA.

2.2.3. Criteria Summary

To locate candidate events, we first restrict the search region to $3.5 \leq L \leq 8$ and search for all points for which the P6 channel reaches 7 counts per second (cps) or above. If the event is a single data spike and is less than 9 cps, it is dismissed as possible noise. If the event is longer, we check to determine whether the P5 channel reaches 2 cps more than twice during the event or in the 20 s window on either side of the event. If so, we dismiss the candidate to ensure that there are no high-energy protons in the area, which could indicate a solar energetic proton event. To exclude penetrating particles and noise, we require that the E3 channel has counts greater than those in the P6 channel. These criteria are summarized in Table 2.

Figure 3 shows several sample events found using the described criteria. Note the low counts in P5 and elevated counts in both P6 and E3 throughout each event. Figure 4 shows two sample rejected event candidates. The candidate in Figure 4a is rejected due to high P5 counts, likely occurring during a solar proton event. The candidate in Figure 4b is rejected due to having counts in E3 below those in P6, and so is classified as possible noise or penetrating particles.

Table 2
REP Event Detection Algorithm Criteria

Criterion	Conditions	Justification
$P6 \geq 7\,\mathrm{cps}$	• At least once during event • For single spikes, $P6 \geq 9\,\mathrm{cps}$	• Well above noise levels
$P5 < 2\,\mathrm{cps}$	• True throughout event and for surrounding ± 10 data points • Allowed one point exception	• Avoid solar proton event and SAA contamination
$E3 \geq P6$	• True for entire event, excluding endpoints	• Avoid penetrating particles • Avoid noise false positives
$3.5 \leq L \leq 8$	• True throughout event	• BLC-only region • Exclude open field lines

Our search criteria are conservative, potentially discarding some real events to avoid admitting false positives. In particular, these criteria will fail to detect weak events, when particle counts do not exceed $7\,\mathrm{cps}$, and high-energy events for which P6 counts would be expected to exceed E3 counts.
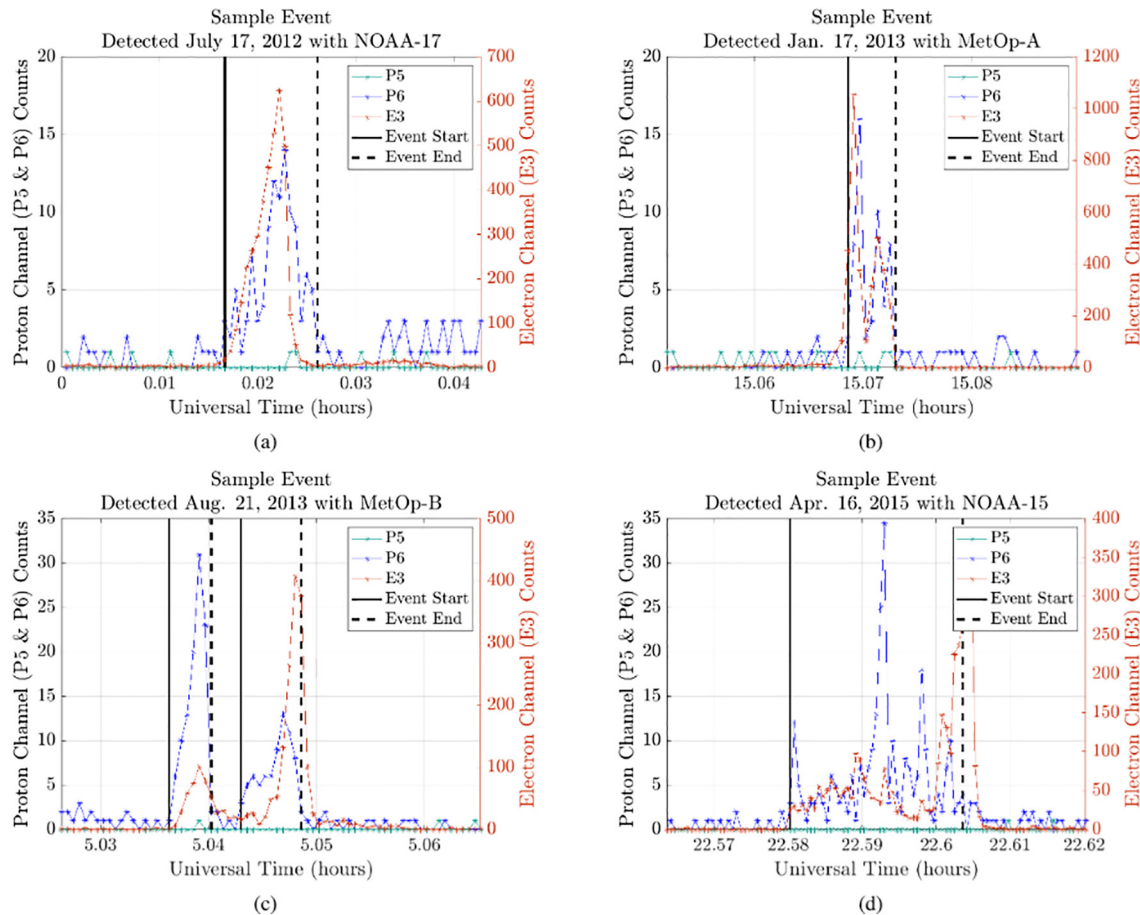

Figure 3. Sample REP events found using multichannel criteria. Counts in the P5 teal and P6 (blue) channels are displayed on the left axis while E3 counts red are displayed on the right hand axis. The event start and end times as determined by the detection algorithm are shown by the solid and dotted black lines, respectively. Panel (c) shows two events in close proximity. REP, relativistic electron precipitation.
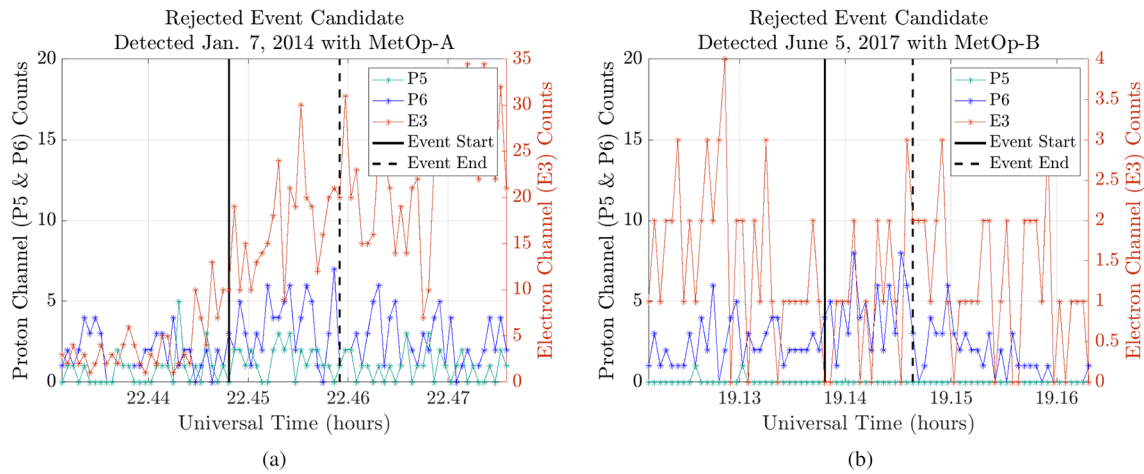
Figure 4. Sample rejected candidate events. Counts in the P5 (teal) and P6 (blue) channels are displayed on the left *y* axis while E3 counts (red) are displayed on the right *y*-axis. The event start and end times as determined by the detection algorithm are shown by the solid and dotted black lines, respectively. (a) Candidate rejected due to high P5 channel counts, indicating a likely solar proton event. (b) Candidate rejected due to low E3 counts, which remain below P6 counts throughout the event, meaning the detection is possibly noise or penetrating particles.

2.2.4. *dL* Calculation

In order to determine the extent of each event in *L* shell (*dL*), it is necessary to define a start and an end for each event. If the counts drop well below the noise level for more than four data points (8 s) surrounding an event, we consider that to be the end of an event. This corresponds to a minimum separation of roughly 50 km between events.

Once the search algorithm identifies a candidate event, where the P6 channel reached at least 7 cps, the default start and end of the event are defined to be the two points surrounding the identified candidate point. The minimum extent of an event is thus taken to be 4 s, spanning three data points. Note that, for single spikes, this gives only an upper limit on the event's extent, amounting to a minimum resolution of ∼0.01 *L*.

The search algorithm then examines the P6 channel counts surrounding the candidate event. We adjust the event end points until all points within three data points of the current end point are well below the noise floor. Since elevated counts near a true event are less likely to be noise than they would be in isolation, we adjust the acceptable noise floor according to how close a point is to points already determined to be part of an event. We thus adopted noise floors of 3, 4, and 5 cps for the points within one, two, and three data points of the current end point, respectively. At the first point for which none of the nearby data points are above the noise floor, the algorithm stops and deems that point to be an end point of the event. If one candidate event ends within three points of the start of another candidate, the candidates are treated together as a single event.

After trying several different methods of determining the start and end of events, examining samples of events found by the algorithm, the above method was found to best match what would be determined by eye.

The *L* value at the start and end points is then determined using the International Geomagnetic Reference Frame (IGRF) magnetic field model. The extent in *L* (*dL*) is taken to be the absolute value of the difference between the *L* value at the start and end of the event.

The IGRF model includes higher-order multipole terms for the magnetic field, but does not account for external current systems or changing geomagnetic conditions (Millan & Baker, 2012). Although more accurate models are available, we use this model to be consistent with the analysis used in Shekhar et al. (2017). However, it is important to note that the IGRF model can be inaccurate especially for the magnetotail during disturbed geomagnetic conditions, which would lead to a likely underestimate in our *dL* determination for events around midnight MLT.
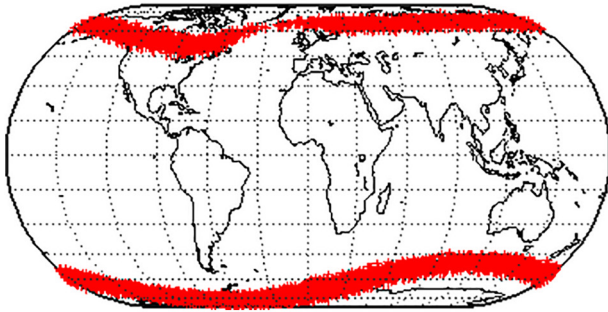
Geographic Distribution of REP Events

Figure 5. Geographic representation of the location of all REP events found in this study. Each event is represented by a single red point at the event's starting location. Events are constrained within the outer radiation belt region. REP, relativistic electron precipitation.

2.2.5. Comparison With Selection Criteria From Shekhar et al. (2017)

Using the averaged 16 s POES/MetOp data, Shekhar et al. (2017) searched for a uniquely defined peak in the P6 channel every 30 min, requiring that the peak exceed 2.5 cps and that at least one consecutive point exceeded 1.5 cps. They required the P5 channel counts to be less than 1% of those recorded in P6, and discarded any events for which E3 < P6. They imposed the same L shell range used in the present study, requiring $3.5 \leq L \leq 8$. When these criteria were met, they took the first and last points above 1.5 cps to define the start and end of the REP event.

The criteria in the present study allow much shorter event durations, and thus higher-resolution in the extent of the event in L. In Shekhar et al. (2017), the minimum L resolution is 0.13 L shells, while in the present study it is ~0.01 L shells. Low-power events that consist of a single or a few elevated P6 data points over a short period of time will likely be picked up by our criteria and ignored by the 16 s data criteria. Additionally, the 16 s criteria may ignore short events (such as single spikes) even if they have very elevated count rates if there is not a consecutive point with a 16 s average count rate above 1.5 cps. These events would be picked up by the 2 s data criteria. Our criteria also allow detection of more than one event during a single pass through the outer radiation belt. It is possible that the 16 s data criteria will pick up some events ignored by our 2 s criteria. For example, an extended period of P6 channel counts that do not exceed 7 cps but still average to more than 2.5 cps in a 16 s window would register as an event in Shekhar et al. (2017), but not in the present study. These may represent extended, weak events.

3. Results

Using the multichannel criteria algorithm on the POES/MetOp SEM-2 data, we found 9,677 events in the period 2012–2018. The geographic distribution of events is shown in Figure 5. Events are constrained within the outer radiation belt region. Due to the asymmetry of the Earth's magnetic field, the density of events is not constant throughout the region. In particular, the magnetic field in the Atlantic is weaker in the Southern Hemisphere than in the Northern Hemisphere. As a result, particles mirror lower in the Southern Hemisphere and so are lost more frequently there and less frequently in the Northern Hemisphere, as is clear from Figure 5.

Additionally, we investigated the distribution of events with respect to the magnetic coordinates L and MLT. Figure 6a shows the raw event distribution: the total number of events found in each L-MLT bin. However, it is important to note that the satellites do not spend equal amounts of time at each magnetic coordinate. Rather, they spend more time at lower L values and certain MLTs, based on the orbit of each individual satellite (Carson et al., 2013). Figure 6b shows the total number of data points taken in each L-MLT for all satellites during the period investigated. Since events are more likely to be observed in regions where the satellites spend more time, we use this distribution to normalize our results, removing the observational bias. The final normalized distribution is presented in Figure 6c.

We find that the majority of events occur in the evening and night sectors, between ~19 and 2 MLT. This is consistent with observations from previous satellite and balloon-based studies, particularly those investigating events driven by electromagnetic ion-cyclotron (EMIC) waves (e.g., Carson et al., 2013; Yahnin et al., 2016). This MLT distribution is also consistent with that reported in Shekhar et al. (2017). The events observed at different MLTs could be consistent with precipitation caused by EMIC waves or whistler-mode chorus waves (Millan & Thorne, 2007). We also find that events are concentrated in the center of our L shell range, mainly between $L = 4$ and $L = 7$, corresponding (as expected) to the heart of the outer radiation belt.

The results of the analysis to determine the spatial extent of REP events in L shell are presented in Figure 7, both with respect to L (Figure 7a) and MLT (Figure 7b). Both of these figures are normalized with respect to the amount of time the satellites collectively spent at each location. We find a single cluster of events
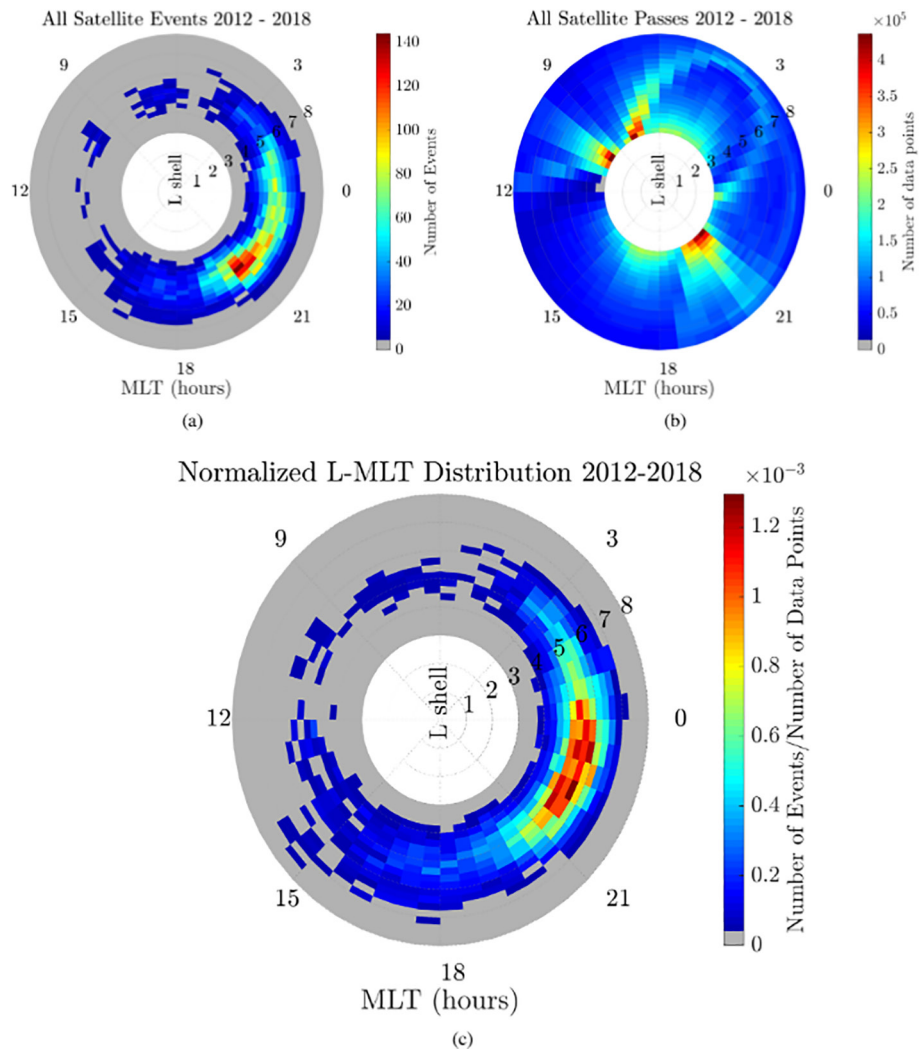
Figure 6. *L*-MLT summary plots. *L* increases radially from the center of the plot and MLT is represented azimuthally, with midnight on the right and noon on the left of each plot. The plots show (a) the total number of REP events detected in each *L*-MLT bin using the POES/MetOp Satellite event detection algorithm, (b) the total amount of data points available in each *L*-MLT bin, representing the amount of time the satellites spent at each location, and (c) the normalized *L*-MLT event distribution, taken by dividing the number of events observed in each bin by the total number of data points available in that bin. Bins without a significant number of counts are shown in gray. REP, relativistic electron precipitation; MLT, magnetic local time.

which are highly localized in L, with the majority less than $0.2 L$ shells wide, which is near the minimum resolvable event size in the study by Shekhar et al. (2017).

Unlike Shekhar et al. (2017), we do not observe a cluster of spatially broad ($dL > 1$) events around midnight MLT. The list of events from Shekhar et al. (2017) as well as the events from this study are available as supplemental information. We compared events from that study to this one for 2013–2014, the 2 years of overlap. We find that, on average, one event in the 16 s data corresponds to a single event in the 2 s data. However, when examining only spatially broad events around midnight MLT in the 16 s data, we find that they correspond to an average of two events in the 2 s data.

Figure 8 shows a representative sample of a broad event detected in the 16 s data. Note that a single long event in the 16 s data corresponds here to two shorter events in the 2 s data. The elevated counts between roughly 2.5 and 2.54 UT were disqualified as an event due to low counts in the E3 channel. Since multiple precipitation mechanisms may act around midnight MLT (Millan & Thorne, 2007), it is possible that the
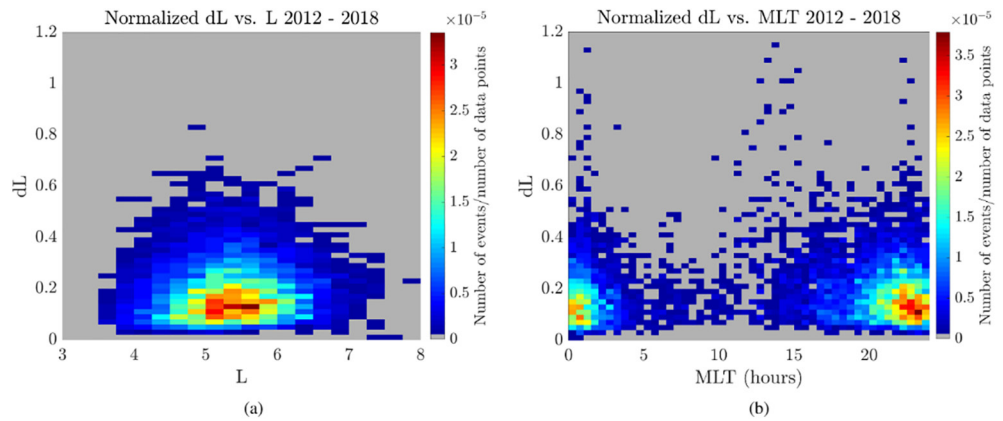
Figure 7. REP event distributions with respect to *dL*. Note that *dL* < 0.2 for the majority of events, suggesting that events are highly localized in *L*. (a) Number of events per number of data points in each *L* bin, integrated over all MLTs. The majority of events occur between *L* = 5–6, in the heart of the outer radiation belt. (b) Number of events per number of data points in each MLT bin, integrated over all *L* shells. The majority of events occur between 20 and 2 MLT, in the evening and night sectors. Bins without a significant amount of counts are shown in gray. REP, relativistic electron precipitation; MLT, magnetic local time.

spatially broad cluster of events near midnight MLT reported by Shekhar et al. (2017) in fact represent precipitation regions composed of multiple events which may have separate causes.

4. Conclusion and Future Work

Using POES/MetOp Satellite 2 s data, we report a single cluster of REP events concentrated in the evening and night sectors MLT and highly localized in *L* shell. This MLT distribution is similar to that reported by Carson et al. (2013), who specifically investigated REP events driven by EMIC waves, although it is possible that the events observed here have multiple sources, not clearly separable by MLT or spatial resolution.
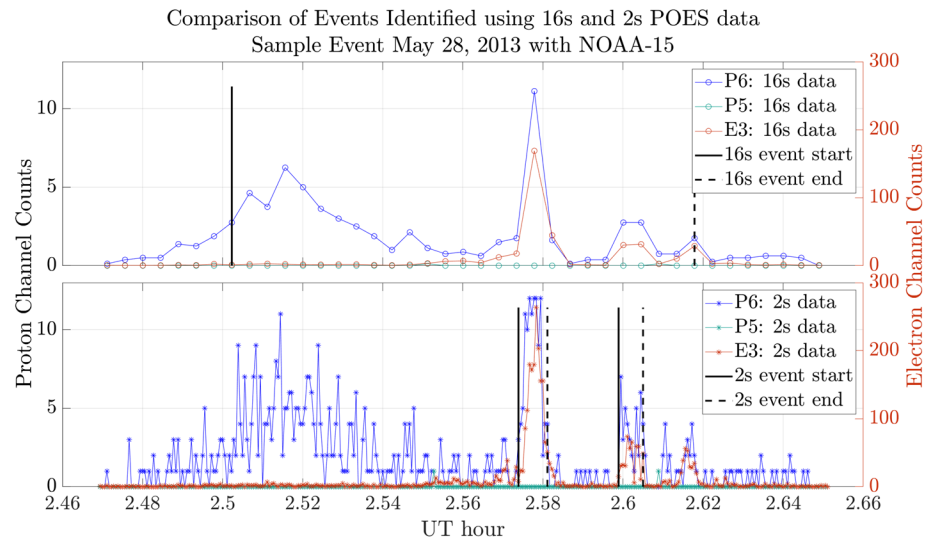

Figure 8. Sample REP event detected with NOAA-15 on May 28, 2013, shown with both the 16 s data (above) and the 2 s data (below). The P5 and P6 channel counts (teal and blue, respectively), are measured on the left *y*-axis, while the E3 channel counts (red) are measured on the right *y* axis. The vertical lines denote the start (solid) and end (dashed) of an event, shown in black. The event occurred around 23.6 MLT, close to midnight. Note that the single precipitation region identified in the 16 s data corresponds to two shorter individual events in the 2 s data. REP, relativistic electron precipitation; MLT, magnetic local time.

The majority of events found have $dL < 0.2$. Blum et al. (2016) reported that the spatial extent of EMIC waves ranges between 0.02 and one in L, which is consistent with the extent of events found in this study. The spatial extent of events we report is consistent with one cluster of events found by Shekhar et al. (2017). However, we do not observe the more spatially extended cluster of events that Shekhar et al. (2017) reported around midnight MLT, possibly because extended events in 16 s data appear as several separate events in 2 s data.

This study faced several limitations, which could be resolved with future work. First, we only examine data from the period 2012–2018, which does not encompass an entire solar cycle. It was therefore not possible to analyze the dependence of events on the solar cycle. However, unprocessed 2 s SEM-2 data exists extending as far back as 1998, when NOAA-15 was launched. This unprocessed data is readily available, and it may be possible to process them into a usable format for a future study. This could allow analysis for nearly two solar cycles, including during a much more active solar period.

Additionally, it is important to note that the dL reported using the event selection criteria represents a maximum extent for each individual event based on the algorithm for finding event start/end times. Currently, dL is calculated using the International Geomagnetic Reference Frame (IGRF) magnetic field model, included in the MEPED data files. However, while this model includes higher-order multipole terms for the magnetic field, it does not account for external current systems or changing geomagnetic conditions (Millan & Baker, 2012). Usually, IGRF is an effective model close to the surface of the Earth, but it can be inaccurate especially on the stretched nightside during disturbed geomagnetic conditions. Thus, future work will implement a magnetic field model that more accurately captures the stretching of Earth's magnetotail, such as the T-89 model (Tsyganenko, 1989).

Finally, future work will undertake additional efforts to connect individual events to their driving precipitation mechanisms. Since EMIC wave associated REP events are usually accompanied by low-energy proton precipitation, future work will examine whether the events detected in this study occur simultaneously with precipitation in the MEPED P1 channel. Data from spacecraft such as the Van Allen Probes, which directly measure disturbances in the magnetic field, can be examined in conjunction with the event list found in this study.

Data Availability Statement

Data available from https://satdat.ngdc.noaa.gov/sem/poes/data/. All data reduction and analysis were performed using MATLAB, licensed by Dartmouth College.

References

Asikainen, T., & Mursula, K. (2011). Recalibration of the long-term NOAA/MEPED energetic proton measurements. *Journal of Atmospheric and Solar-Terrestrial Physics*, *73*(2–3), 335–347. https://doi.org/10.1016/j.jastp.2009.12.011

Asikainen, T., Mursula, K., & Maliniemi, V. (2012). Correction of detector noise and recalibration of NOAA/MEPED energetic proton fluxes. *Journal of Geophysical Research*, *117*, A09204. https://doi.org/10.1029/2012JA017593

Blum, L. W., Agapitov, O., Bonnell, J. W., Kletzing, C., & Wygant, J. (2016). Emic wave spatial and coherence scales as determined from multipoint van allen probe measurements. *Geophysical Research Letters*, *43*, 4799–4807. https://doi.org/10.1002/2016GL068799

Brasseur, G., & Solomon, S. (2005). *Aeronomy of the middle atmosphere 3rd revised and enlarged*. New York: Springer.

Capannolo, L., Li, W., Ma, Q., Shen, X.-C., Zhang, X.-J., Redmon, R., et al. (2019). Energetic electron precipitation: Multi-event analysis of its spatial extent during emic wave activity. *Journal of Geophysical Research: Space Physics*, *124*, 2466–2483. https://doi.org/10.1029/2018JA026291

Carson, B. R., Rodger, C. J., & Clilverd, M. A. (2013). POES satellite observations of EMIC-wave driven relativistic electron precipitation during 1998-2010. *Journal of Geophysical Research: Space Physics*, *118*, 232–243. https://doi.org/10.1029/2012JA017998

Evans, D. S., & Greer, M. S. (2000). *Polar orbiting environmental satellite space environment monitor-2: Instrument description and archive data documentation*. Boulder, CO: US Department of Commerce, National Oceanic and Atmospheric Administration.

Green, J. (2013). MEPED telescope data processing algorithm theoretical basis document. Boulder, CO: National Oceanic and Atmospheric Administration Space Environment Center.

Horne, R. B., Glauert, S. A., Meredith, N. P., Koskinen, H., Vainio, R., Afanasiev, A., et al. (2013). Forecasting the Earth's radiation belts and modeling solar energetic particle events: Recent results from SPACECAST. *Journal of Space Weather and Space Climate*, *3*, A20. https://doi.org/10.1051/swsc/2013042

Horne, R. B., Lam, M. M., & Green, J. C. (2009). Energetic electron precipitation from the outer radiation belt during geomagnetic storms. *Geophysical Research Letters*, *36*, L19104. https://doi.org/10.1029/2009GL040236

Lenchek, A. M., & Singer, S. F. (1962). Geomagnetically trapped protons from cosmic-ray albedo neutrons. *Journal of Geophysical Research*, *67*(4), 1263–1287.

McFadden, J. P., Evans, D. S., Kasprzak, W. T., Brace, L. H., Chornay, D. J., & Coates, A. J., et al. (2007). In-flight instrument calibration and performance verification. *Calibration of Particle Instruments in Space Physics*, 7, 277–385.

Meredith, N. P., Thorne, R. M., Horne, R. B., Summers, D., Fraser, B. J., & Anderson, R. R. (2003). Statistical analysis of relativistic electron energies for cyclotron resonance with emic waves observed on CRRES. *Journal of Geophysical Research*, 108(A6), 1250. https://doi.org/10.1029/2002JA009700

Millan, R., Yando, K., Green, J., & Ukhorskiy, A. (2010). Spatial distribution of relativistic electron precipitation during a radiation belt depletion event. *Geophysical Research Letters*, 37, L20103. https://doi.org/10.1029/2010GL044919

Millan, R. M., & Baker, D. N. (2012). Acceleration of particles to high energies in earth's radiation belts. *Space Science Reviews*, 173(1–4), 103–131. https://doi.org/10.1007/s11214-012-9941-x

Millan, R. M., & Thorne, R. M. (2007). Review of radiation belt relativistic electron losses. *Journal of Atmospheric and Solar-Terrestrial Physics*, 69(3), 362–377. https://doi.org/10.1016/j.jastp.2006.06.019

Miyoshi, Y., Sakaguchi, K., Shiokawa, K., Evans, D., Albert, J., Connors, M., & Jordanova, V. (2008). Precipitation of radiation belt electrons by emic waves, observed from ground and space. *Geophysical Research Letters*, 35, L23101. https://doi.org/10.1029/2008GL035727

Nesse Tyssøy, H., Sandanger, M. I., Ødegaard, L.-K., Stadsnes, J., Aasnes, A., & Zawedde, A. (2016). Energetic electron precipitation into the middle atmosphere—Constructing the loss cone fluxes from MEPED POES. *Journal of Geophysical Research: Space Physics*, 121, 5693–5707. https://doi.org/10.1002/2016JA022752

O'Brien, B. J. (1964). High-latitude geophysical studies with satellite Injun 3: 3. Precipitation of electrons into the atmosphere. *Journal of Geophysical Research*, 69(1), 13–43.

Peck, E. D., Randall, C. E., Green, J. C., Rodriguez, J. V., & Rodger, C. J. (2015). POES MEPED differential flux retrievals and electron channel contamination correction. *Journal of Geophysical Research: Space Physics*, 120, 4596–4612. https://doi.org/10.1002/2014JA020817

Qin, M., Hudson, M., Millan, R., Woodger, L., & Shekhar, S. (2018). Statistical investigation of the efficiency of emic waves in precipitating relativistic electrons. *Journal of Geophysical Research: Space Physics*, 123, 6223–6230. https://doi.org/10.1029/2018JA025419

Randall, C., Harvey, V., Manney, G., Orsolini, Y., Codrescu, M., & Sioris, C., et al. (2005). Stratospheric effects of energetic particle precipitation in 2003–2004. *Geophysical Research Letters*, 32, L05802. https://doi.org/10.1029/2004GL022003

Rodger, C. J., Clilverd, M. A., Green, J. C., & Lam, M. M. (2010). Use of poes sem-2 observations to examine radiation belt dynamics and energetic electron precipitation into the atmosphere. *Journal of Geophysical Research*, 115, A04202. https://doi.org/10.1029/2008JA014023

Sandanger, M., Søraas, F., Aarsnes, K., Oksavik, K., & Evans, D. (2007). Loss of relativistic electrons: Evidence for pitch angle scattering by electromagnetic ion cyclotron waves excited by unstable ring current protons. *Journal of Geophysical Research: Space Physics*, 112, A12213. https://doi.org/10.1029/2006JA012138

Selesnick, R. (2006). Source and loss rates of radiation belt relativistic electrons during magnetic storms. *Journal of Geophysical Research*, 111, A04210. https://doi.org/10.1029/2005JA011473

Shekhar, S., Millan, R., & Smith, D. (2017). A statistical study of the spatial extent of relativistic electron precipitation with polar orbiting environmental satellites. *Journal of Geophysical Research: Space Physics*, 122, 11274–11284. https://doi.org/10.1002/2017JA024716

Shprits, Y. Y., Subbotin, D. A., Meredith, N. P., & Elkington, S. R. (2008). Review of modeling of losses and sources of relativistic electrons in the outer radiation belt ii: Local acceleration and loss. *Journal of Atmospheric and Solar-Terrestrial Physics*, 70(14), 1694–1713. https://doi.org/10.1016/j.jastp.2008.06.014

Summers, D., Thorne, R. M., & Xiao, F. (1998). Relativistic theory of wave-particle resonant diffusion with application to electron acceleration in the magnetosphere. *Journal of Geophysical Research*, 103(A9), 20487–20500.

Thorne, R. M., & Andreoli, L. J. (1980). Mechanisms for intense relativistic electron precipitation. In *Exploration of the polar upper atmosphere* (pp. 381–394). Berlin: Springer. https://doi.org/10.1007/978-94-009-8417-2_31

Thorne, R. M., O'Brien, T., Shprits, Y., Summers, D., & Horne, R. B. (2005). Timescale for MeV electron microburst loss during geomagnetic storms. *Journal of Geophysical Research*, 110, A09202. https://doi.org/10.1029/2004JA010882

Tsyganenko, N. A. (1989). A magnetospheric magnetic field model with a warped tail current sheet. *Planetary and Space Science*, 37(1), 5–20. https://doi.org/10.1016/0032-0633(89)90066-4

Van de Kamp, M., Seppälä, A., Clilverd, M. A., Rodger, C. J., Verronen, P., & Whittaker, I. (2016). A model providing long-term data sets of energetic electron precipitation during geomagnetic storms. *Journal of Geophysical Research: Atmospheres*, 121, 12–520. https://doi.org/10.1002/2015JD024212

Yahnin, A. G., Yahnina, T. A., Semenova, N. V., Gvozdevsky, B. B., & Pashin, A. B. (2016). Relativistic electron precipitation as seen by NOAA poes. *Journal of Geophysical Research: Space Physics*, 121, 8286–8299. https://doi.org/10.1002/2016JA022765

Yando, K., Millan, R. M., Green, J. C., & Evans, D. S. (2011). A Monte Carlo simulation of the NOAA POES medium energy proton and electron detector instrument. *Journal of Geophysical Research*, 116, A10231. https://doi.org/10.1029/2011JA016671